Oxidation of Ir(111): From O−Ir−O Trilayer to Bulk Oxide Formation

Y. B. He,[†,‡,||] A. Stierle,[*,‡] W. X. Li,[*,§] A. Farkas,[†] N. Kasper,[‡] and H. Over[*,†]

Department of Physical Chemistry, Justus-Liebig-University, Heinrich-Buff Ring 58, D-35392 Giessen, Germany, Max-Planck Institut für Metallforschung, Heisenbergstr. 3, D-70569 Stuttgart, Germany, and State Key Laboratory of Catalysis, Dalian Institute of Chemical Physics, Chinese Academy of Sciences, 457 Zhongshan Road, Dalian 116023, China

Received: April 24, 2008; Revised Manuscript Received: May 13, 2008

The oxidation of the Ir(111) surface was studied by in situ surface X-ray diffraction (SXRD) in an oxygen pressure range of 10^{-6}−100 mbar at temperatures from 575 to 875 K, in combination with density functional theory calculations. Depending on the partial pressure and temperature, the formation of a series of oxide phases is observed. At a sample temperature of 575 K, a single O−Ir−O trilayer forms at oxygen pressures of 10^{-3} to 1 mbar, which grows into a hexagonal multilayer surface oxide at pressure of 100 mbar. Both surface oxides are only kinetically stabilized structures according to DFT calculations. The multilayer surface oxide is kinetically very stable against decomposition in vacuum and further oxidation at low temperature of 575 K as revealed by SXRD. At higher sample temperatures (775 and 875 K), O−Ir−O trilayers form at pressures around 1 mbar, whereas at a pressure of 100 mbar, bulklike rutile IrO_2 grows with predominant orientations of (110) and (100) along the normal of Ir(111).

1. Introduction

In recent years, much research effort has been devoted to achieve a fundamental understanding of the oxidation of late transition and noble metals at high oxygen pressures and elevated temperatures.[1] This interest was triggered by the finding that surface oxide phases can play a crucial role in oxidation catalysis.[2] As the oxides of noble metals form only at rather high oxygen partial pressures and elevated temperatures, they have often been overlooked when metal surfaces are studied under ultrahigh vacuum (UHV) conditions. Combing UHV based and atmospheric pressure compatible experimental techniques[3] with state-of-the-art density functional theory (DFT) calculations, the oxidation of a number of noble metals such as Ru,[4,5] Rh,[6] Pd,[7] and Pt[8] have been carefully studied, resolving not only the complex structure of the formed surface or bulk oxides as well as their electronic and reactivity properties but also providing us with an atomic-scale understanding on the initial oxidation processes.

Iridium is considered as a promising candidate for the catalytic reduction of NO to N_2 under excess oxygen conditions which is encountered in the after-treatment of the exhaust gases of energy-efficient engines.[9] Unfortunately, the oxidation of Ir impairs this reduction propensity so that a detailed understanding of the oxidation process of Ir is mandatory for the application of iridium in future three-way catalytic converters.[10] Although oxygen chemisorption on the Ir(111) has been fairly well studied,[11−16] oxidation of the Ir(111) has hitherto been rarely investigated.[17] In the present work we have studied the initial oxidation of the Ir(111) surface using in situ surface X-ray diffraction (SXRD) at oxygen partial pressures ranging from 10^{-6} to 100 mbar. For studying the oxidation at pressures beyond UHV or high vacuum regime, conventional surface science techniques may still be used, but have to be ex situ, i.e., oxidizing the sample at high pressures but characterization in UHV. The recently developed technique of high-pressure SXRD is well suited for in situ characterization of surface changes under high pressure environments due to a negligible interaction between the X-rays and the gas atmosphere.[18] With SXRD, we followed in situ and on the atomic scale the evolution of the Ir(111) surface under oxygen pressures ranging from 10^{-6} mbar up to ambient pressure at various temperatures. The oxidation process of Ir(111) starts with a single O−Ir−O trilayer, which is followed by a hexagonal multilayer oxide and finally results in the formation of bulklike rutile IrO_2. Our experimental results are complemented by DFT calculations.

2. Experimental and Computational Details

The SXRD measurements were carried out at the dedicated MPI-MF beamline at Ångstrøm Quelle Karlsruhe (ANKA), Germany.[19] A photon energy of 9 keV ($\lambda = 1.3776$ Å) was used, and the experiments were conducted in a six-circle diffraction mode. The incident angle was fixed at 0.48°, close to the Ir total reflection angle. The crystal basis used to describe the (H, K, L) diffraction is a hexagonal basis set ($\mathbf{a}_1$, $\mathbf{a}_2$, $\mathbf{a}_3$), with $\mathbf{a}_1$ and $\mathbf{a}_2$ lying in the surface plane and being of equal length $a_0/\sqrt{2}$, and with $\mathbf{a}_3$ directing out of plane with length $\sqrt{3}a_0$ [a_0 (Ir) = 3.84 Å], cf. Figure 1. The sample was mounted on an Inconel sample holder in a UHV compatible X-ray diffraction chamber, which allows oxygen partial pressures of up to 10^3 mbar and temperatures up to 1100 K using an Al_2O_3 encapsulated radiative heater. The temperature was measured by a type K thermocouple spot-welded to the sample (uncertainty ± 3 K). The Ir(111) sample surface was cleaned by Ar-ion sputtering followed by annealing at ≈1050 K for a few minutes. The oxidation of the Ir(111) surface was monitored in situ by SXRD while exposing the sample to various O_2 partial

---

* Corresponding authors. E-mail: Herbert.Over@phys.Chemie.uni-giessen.de (Herbert Over), stierie@mf.mpg.de (Andreas Stierle), and wxli@dicp.ac.cn (Wei-Xue Li). Fax: +49-641-9934559. URL: http://www.chemie.uni-giessen.de/home/over.

[†] Justus-Liebig-University.

[‡] Max-Planck Institut für Metallforschung.

[§] Chinese Academy of Sciences.

[||] Present address: Faculty of materials science and engineering, Hubei University, 11 Xueyuan Road, Wuchang, Wuhan 430062, China.

10.1021/jp803607y CCC: $40.75

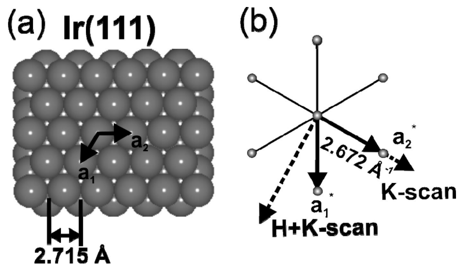

Figure 1. (a) Schematic illustration of the Ir(111) surface in real space and the corresponding reciprocal lattice (b). The real-space and reciprocal lattice vectors, 2.715 Å and $2\pi/[2.715 \times (\sqrt{3/2})] = 2.672$ Å^{-1} in length, respectively, as well as the K-scan and H+K-scan directions probed during the SXRD experiments are indicated.

pressures (ranging from 10^{-6} mbar to some 100 mbar) at sample temperatures between 575 and 875 K.

Density functional theory calculations were carried out using the ultrasoft pseudopotential plane wave code (DACAPO), in which Ir 5d electrons were treated as part of the valence electrons, and wave functions were expanded by the plane wave basis set with a kinetic cutoff of 25 Ry.[20] The generalized-gradient Perdew−Wang91 functional was used to approximate the exchange-correlation interaction.[21] The surface Brillouin zone sampling was carried out with a (4 × 4 × 1) grid in the Monkhorst-Pack[22] scheme for the (2 × 2) unit cell and adjusted for other surfaces with different unit cells accordingly. We used a five layer slab geometry with an optimized lattice constant of 3.86 Å (compared to experimental value 3.84 Å) to model various structures, and the top two Ir layers and adsorbates were fully relaxed in response to their surface environment, whereas the rest of the atoms was fixed at their bulk positions.[23] All total energies have been extrapolated to $k_BT = 0$ eV. The oxygen adsorption energy (averaged) is defined by

$$E_{ads}(\theta) = [E(\mathrm{O,Ir}) - 0.5NE(\mathrm{O_2}) - E(\mathrm{Ir,slab})]/N$$

where $E(\mathrm{O,Ir})$, $E(\mathrm{O_2})$, and $E(\mathrm{Ir, slab})$ are the total energy of adsorbate−substrate system, oxygen molecules, and Ir substrates, respectively. N is the number of adsorbed oxygen atoms. Here a positive (negative) value indicates that adsorption is endothermic (exothermic). The effects of temperature and pressure were considered by so-called ab initio thermodynamics,[24,25] and the Gibbs free energy of formation per Å^2 for oxygen adsorption on Ir(111) was approximated by

$$\gamma(T,p,\theta) = \theta[E_{ads}(\theta) - 0.5\Delta\mu(T,p)]/A$$

where θ is the oxygen coverage and A is area per (1 × 1) unit cell. $\Delta\mu(T,p) = \Delta\mu(T,p_0) + kT\ln(p/p_0)$ is the chemical potential of oxygen molecules, which is a function of T and oxygen partial pressure p. $\Delta\mu(T,p_0)$ is the temperature dependent oxygen chemical potential at one atmospheric pressure p_0, which is compiled in thermodynamic tables.[26]

3. Results and Discussion

3.1. In Situ SXRD Investigations. We performed a reciprocal space exploration at various oxygen partial pressures and temperatures ranging from 575 to 875 K. The main findings are summarized in Table 1. Figure 2a depicts the in-plane K scan (keeping L fixed at 0.15 reciprocal lattice units (r.l.u.)) when exposing the sample to 8×10^{-2} mbar of O_2 at 575 K. At oxygen partial pressures higher than 10^{-3} mbar, a diffraction peak is observed at (0, 0.87, 0.15) indicating the formation of a new structure on the surface. In addition, a peak is observed in the $H + K$ scan at $H = K = 0.87$, implying the formation of a hexagonal structure. While exposing the Ir(111) sample to $10^{-6}-10^{-3}$ mbar of O_2 at 575 K, a gradual increase of the peak signal in the K scan is detected. The 6-fold symmetry is directly confirmed by a θ scan at (0, 0.87, 0.15), rotating the sample around its surface normal, as shown in the inset of Figure 2a. To probe the 3D structure of the newly formed layer, a scan along L was performed at (0, 0.87), as indicated in Figure 2b (red line). Upon progressing oxidation, a clear increase of the signal can be observed over the whole L range. For comparison, a reference scan for the clean surface at 575 K is given (black line). The peak close to $L = 2$ is a tail of the Ir bulk Bragg reflection at (0,1,2). After subtraction of the Ir Bragg peak tail measured on the clean surface, the resulting signal is given in the inset of Figure 2 b. The absence of well-defined peaks and the smooth decrease of the intensity with increasing L are indicative of a single Ir layer being involved in the diffraction process. It is therefore likely (and will be confirmed later) that a single O−Ir−O trilayer with 6-fold symmetry grows on the Ir(111) surface under such conditions, resembling the initial

TABLE 1: Summary of the Oxidation Conditions and the Resulting Phases on the Ir(111) as Observed by SXRD

T/K	$P(\mathrm{O_2})$/mbar	phase
575	$10^{-6}-10^{-4}$	chemisorbed O
	$10^{-3}-1$	O−Ir−O trilayer
	$10-100$	multilayer oxide
775 (875)	$10^{-5}-10^{-2}$	chemisorbed O
	1	O−Ir−O trilayer
	100	bulklike IrO_2

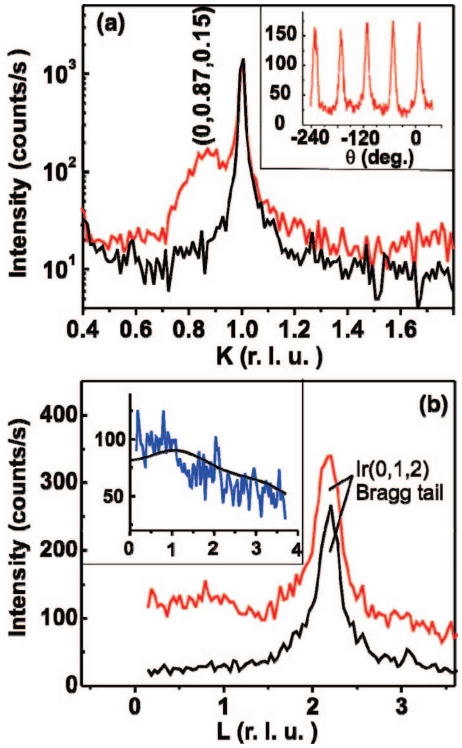

Figure 2. In situ SXRD reciprocal space scans of the Ir(111) surface when exposing the sample to 8×10^{-2} mbar O_2 at 575 K. (a) In-plane K scan with $H = 0$ and $L = 0.15$ r.l.u. and (b) out-of-plane L scan at $(H, K) = (0, 0.87)$ from the oxidized sample (red line) are shown in comparison with those from the clean Ir(111) surface (black line). The inset in (a) is a rocking scan around (0, 0.87, 0.15) from the oxidized surface. The inset in (b) presents the difference L scan of the oxidized and the clean surface, i.e., the L scan from the formed surface oxide layer. The solid line represents the calculated intensity for an O−Ir−O trilayer, based on the DFT atomic positions.

oxidation of Rh(111), where a hexagonal O−Rh−O trilayer surface oxide was identified at a sample temperature above 575 K and O_2 pressures between 10^{-3} and 1 mbar.[6]

From the peak at $K = 0.87$, the in-plane lattice distance of the O−Ir−O trilayer is derived to be 2.715/0.87 = 3.12 Å (2.715 Å is the in-plane Ir(111) interatomic distance). Thus, the layer can be described as a coincidence lattice (6 × 6) hexagonal O−Ir−O trilayer on a (7 × 7) Ir(111) surface unit cell, which was considered as the initial input for the DFT calculations. The peak width (∼0.14) of the reflection at (0, 0.87) corresponds to an in-plane domain size (2.715/0.14 = 19.4 Å) of about one coincidence lattice unit cell which is 19 Å, demonstrating that the layer is laterally poorly ordered. This is also reflected in a θ scan peak width of 8.3°. At 775 K (cf. Table 1), the ordering of the layer is slightly improved, but it is still much less ordered compared to the O−Rh−O coincidence trilayer formed on the Rh(111) surface.[6]

To gain further insight into the atomic structure of the formed surface oxide, out-of-plane crystal truncation rods (CTR) of the clean and oxygen-covered Ir(111) surface were recorded at 575 K, as compiled in Figure 3a.[27] A fit of the data reveals that the Ir(111) surface is bulk terminated with an inward relaxation of the first and second layers by −1.2% and −0.6%, respectively (cf. Figure 3b for the structural model), in good agreement with a low energy electron diffraction (LEED) $I-V$ curve analysis.[28] In addition, the mean square vibrational amplitudes of the surface layer and the subsurface layer are strongly enhanced as compared to the bulk value, in line with a high surface mobility of the Ir atoms at 575 K.

Upon formation of the surface oxide coincidence layer, the CTRs change only slightly, as can be inferred from Figure 3a, lower part. This observation indicates that the surface oxide formation does not involve enhanced mass transport perpendicular to the surface which would result in a roughening induced decrease of the CTR amplitude. The simulation of the structure factor for a (6 × 6) hexagonal O−Ir−O trilayer on a (7 × 7) Ir(111) surface unit cell as motivated by the DFT calculations discussed below, is shown in Figure 3a, lower part (solid lines). In addition the scattered intensity was calculated for the surface rod shown in the inset of Figure 2(b).[29] The good agreement between the measured and calculated rods provides further support for the formation of an O−Ir−O trilayer.

The O−Ir−O trilayer is stable up to an oxygen partial pressure of at least 1 mbar at 575 K. With further increase of the O_2 pressure to 100 mbar, the diffraction signal from the Ir(111) surface (cf. Figure 4) indicates the formation of a multilayer hexagonal oxide.[30] A θ scan at (0, 0.91, 0.15) reveals still a 6-fold symmetry of the present structure. The well-defined peak at $L = 3.12$ in the out-of-plane L-scan at $(H, K) = (0, 0.91)$, see Figure 4(b), indicates that several Ir layers are now contributing to the diffraction signal. From the peak width (∼0.46) the multilayer oxide thickness can be estimated to be 6.649/0.46 = 14.5 Å (6.649 Å is the as-defined out-of-plane lattice vector $\sqrt{3}a_0$). The signal from the surface O−Ir−O layer is still present in the L scan, compatible with a Stranski−Krastanov like growth mode of oxide islands, involving a wetting layer at the surface. Thus, the formation of a multilayer surface oxide (involving several Ir layers) on the Ir(111) surface at low sample temperature but high O_2 partial pressure is clearly identified with SXRD. From the position of the peaks it can be derived that a (0001) oriented corundum Ir_2O_3 layer is formed with $a = 5.168$ Å and $c = 12.78$ Å, which is energetically meta-stable, as will be shown below,[31] but the multilayer oxide formed on Ir(111) is kinetically very stable. The Ir_2O_3 oxide is stable under high vacuum conditions without decomposition at 575 K and it resists further oxidation to bulk oxide in ambient pressure O_2 at a temperature of 575 K on a time scale of hours. However, the multilayer oxide can be readily decomposed at 1050 K in vacuum.

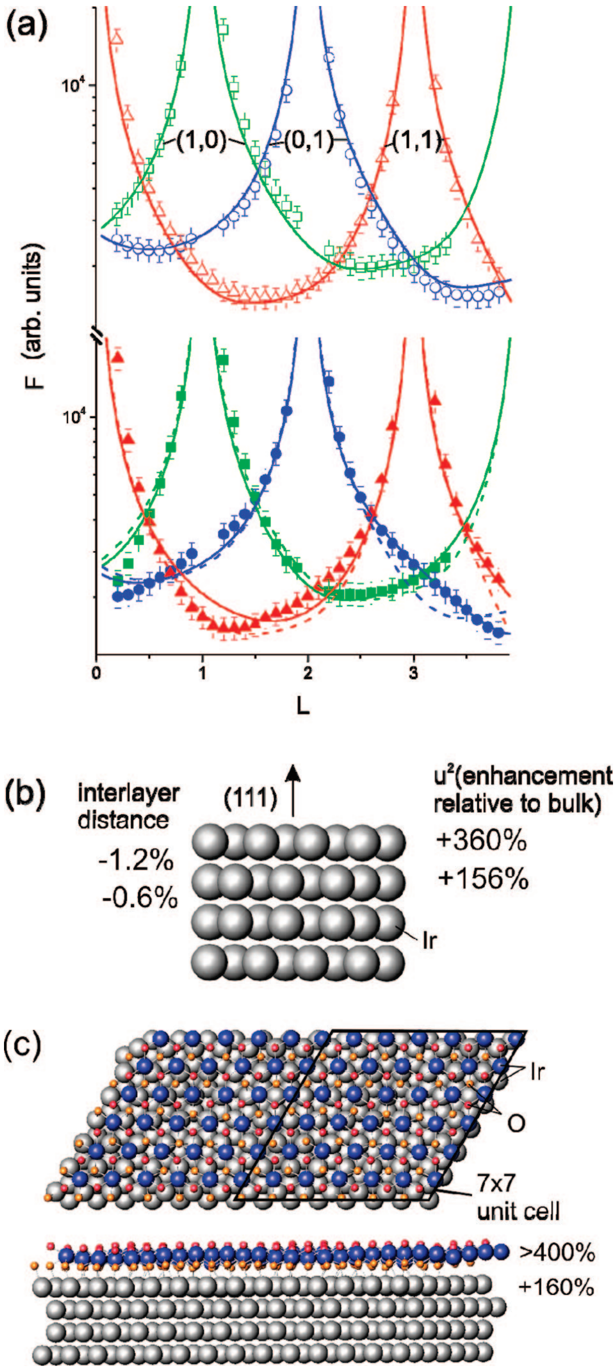

Figure 3. (a) Upper part: CTRs of the clean Ir(111) surface (data points) together with the best fits (solid lines), corresponding to the structural model in (b). Lower part: CTRs of the Ir(111) surface being exposed to 5 × 10^{-2} mbar O_2 at 575 K (data points) together with the calculated structure factor for the O−Ir−O surface oxide (solid line). The dashed line corresponds to the best fit structure factor of the clean surface. (c) Structural model of a (6 × 6) hexagonal O−Ir−O trilayer on a (7 × 7) Ir(111) surface unit cell.

Now we turn to the formation of rutile IrO_2 at higher temperatures, i.e., 775 K and above. In a wide O_2 partial pressure range of 10^{-5}−10^{-2} mbar, no oxide formation was observed.

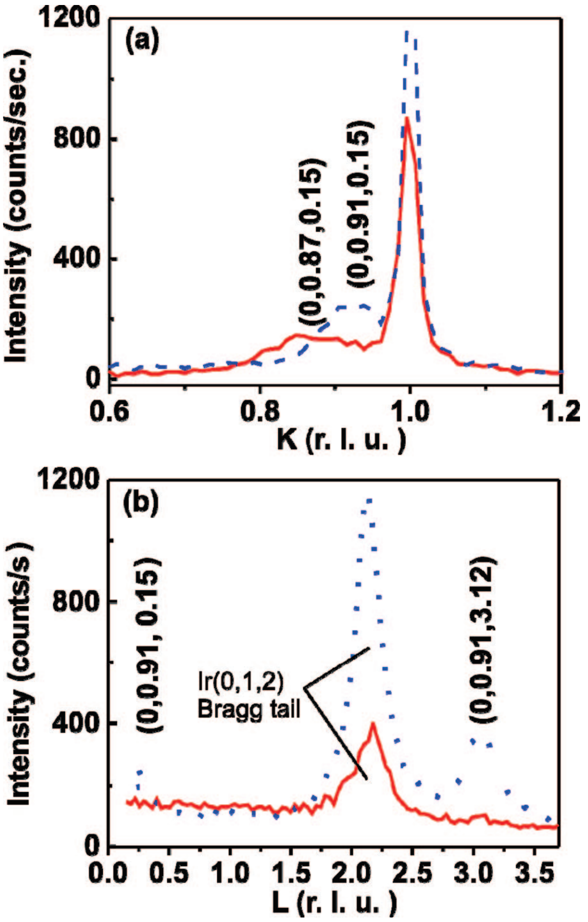

Figure 4. *K* and *L* scans of the Ir(111) surface at 120 mbar O_2 and 575 K (dashed, blue lines) in comparison to the scans taken at 8×10^{-2} mbar of O_2 (solid, red lines). (a) In-plane *K* scans at $(H, L) = (0, 0.15)$: the multilayer oxide exhibits a smaller in-plane lattice constant as compared to the surface oxide. (b) Out-of-plane *L* scans at $(H, K) = (0, 0.91)$ for the multilayer oxide and (0,0.87) for the surface oxide. In the scan of the multilayer oxide, additional Bragg peaks arise at $L \approx 0$ and $L = 3.12$. The tail of the Ir(0,1,2) Bragg reflection is more pronounced, since the scan is closer to $K = 1$ as compared to the scan for the surface oxide.

This finding precludes the oxidation of Ir(111) under typical UHV conditions. At 1 mbar, a single O−Ir−O trilayer grows. Further increase of the O_2 pressure to 100 mbar leads to the formation of stable IrO_2 bulk oxide with rutile structure in (110) and (100) orientations, as we will demonstrate in the following paragraphs. All observed reflections are summarized in Table 2.

In the *K* scan, as presented in Figure 5a, distinct diffraction maxima appear at $K = 0.73$ and 1.47, corresponding to $IrO_2(1\bar{1}0)$ and $(2\bar{2}0)$ reflections. The out-of-plane periodicity is determined from the peak at $L = 2.1$ in the *L* scan at $(H, K) = (0, 0.73)$ (see Figure 5c), corresponding to the $IrO_2(200)$ reflection. The *d* spacing between the IrO_2 planes parallel to the surface can be inferred to be $6.649/2.1 = 3.17$ Å, in good agreement with the bulk layer spacing of $IrO_2(110)$ planes (3.18 Å). These findings point to the epitaxial growth of IrO_2 in (110) orientation (domain type I), with three rotational in-plane domains due to the hexagonal symmetry of the underlying Ir(111) substrate. Additional evidence for the (110) oriented domains comes from the $H + K$ scans exhibiting a dominant peak at $H = K = 0.86$ corresponding to the IrO_2 (002) reflection (not shown here). From the reciprocal-space lattice parameters $K = 0.735$ and $H = K = 0.86$, we derive the (real space) in-plane lattice parameters of the $IrO_2(110)$ domains to be 3.16 Å × 6.39 Å.[32] These values correspond nicely to the bulk-truncated surface unit cell of $IrO_2(110)$, namely, 3.15 Å × 6.36 Å, as expected for an unstrained $IrO_2(110)$ film on the Ir(111) surface. The in-plane reflections from domain type I are plotted in the reciprocal lattice in Figure 6a as green circles. The half-width of the maximum at 0.73 in the K scan is 0.02. Therefore the averaged lateral dimension of the $IrO_2(110)$ domains along the $[1\bar{1}0]$ direction is approximately $2\pi/(2.672 \times 0.02) = 118$ Å. The peak width at 0.86 in the $H + K$ scan is 0.009 which corresponds to a mean domain size of approximately $2\pi/(2.672 \times \sqrt{3} \times 0.009) = 151$ Å along the [001] direction. From the fwhm of (0.08) of the peak (0, 0.73, 2.1) in the *L* scan the average thickness of the $IrO_2(110)$ domains is estimated to be $6.649/0.08 = 83$ Å, i.e., consisting of about 26 IrO_2 layers.

Domain type II exhibits (100) orientation, which is evidenced from the θ scan at (0, 0.91, 0.15), see Figure 5b. The scan exhibits a splitting into two (011) type reflections, which overlap along the (0,1) surface direction. The L scan at $K = 0.91$ (Figure 5c, gray line) exhibits a new reflection close to $L = 3$, corresponding to a tail from the IrO_2 (211) reflection of domain type II (see in-plane reciprocal lattice in Figure 6a). The in-plane (020) peak from the (100) domains is detected as a shoulder ($K = 1.04$) of the (0, 1) CTR from the Ir(111) substrate, which is shown in the inset of Figure 5a. Both types of domains (I + II) are oriented with their [001] direction along the substrate surface (1, 1) direction. In addition, small reflections are observed in all scans, corresponding to IrO_2 powder diffraction peaks.

The in-plane and out-of-plane lattice parameters of the (100) domains are 3.16 Å × 4.52 Å and 2.22 Å, respectively. These values compare well with 3.15 Å × 4.50 Å and 2.25 Å for the bulk-terminated $IrO_2(100)$ structure. From the fwhm of the (0, 0.91, 0.15) peak in the *K* scan (0.037) and that of the peak (0, 0.91, 3.0) in the *L* scan (0.13), the average in-plane size and thickness of the (100) domains are estimated to be $2\pi/(2.672 \times 0.037) = 64$ Å and $6.649/0.13 = 51$ Å, respectively. The reciprocal lattice of Ir(111) is shown in Figure 6 for $L = 0$. The lattices of both IrO_2 (110) and (100) domains are included in the figure. The superposition of (110) and (100) oriented domains of rutile IrO_2 explains all scans shown in Figure 5, confirming that three rotational (100) domains (rotated by 120° with each other) coexist with the three rotational $IrO_2(110)$ domains, as shown in Figure 6b in real space.

The IrO_2 film formed on the Ir(111) surface at high temperature and high O_2 partial pressure is similar to the RuO_2 film grown on Ru(0001). Thicker RuO_2 films also grow in both (110) and (100) orientations on Ru(0001) with three rotational domains.[33] The IrO_2 film has a rutile structure and is predominantly oriented along (110) with the following epitaxial relationship to the Ir(111) substrate: $IrO_2(110) \| Ir(111)$ out of plane, and $IrO_2[001] \| Ir[10\bar{1}]_{bulk}$ and $IrO_2[1\bar{1}0] \| Ir[\bar{1}2\bar{1}]_{bulk}$ in plane. The out-of-plane and the in-plane orientations of the epitaxial (100) domains of the IrO_2 film with respect to the Ir(111) substrate are $IrO_2(100) \| Ir(111)$, $IrO_2[001] \| Ir[10\bar{1}]_{bulk}$, and $IrO_2[0\bar{1}0] \| Ir[\bar{1}2\bar{1}]_{bulk}$, respectively. The IrO_2 bulk oxide can also be prepared by NO_2: The inset displays a LEED pattern of the Ir(111) surface after oxidation with 36 000 L of NO_2 at 600 K. The LEED pattern shown in Figure 6a derived from superimposed reciprocal lattices of $IrO_2(110)$ and (100) domains. The schematic LEED pattern explains directly the splitting of two (011) spots from (100) domains along the surface (0, 1) direction, confirming the above finding by SXRD.

TABLE 2: Identification of the XRD Peaks Shown in the *K*, *H* + *K*, and *L* Scan for the Bulklike IrO_2 Formed at Higher Oxidation Temperature[a]

scan	coordination in reciprocal space	domain	corresponding reflection (planes in real space)
K scan at $(H,L) = (0, 0.15)$; Figure 5a	(0,0.73,0.15)	I	$(1\bar{1}0)$ of IrO_2(110)-domain
	(0,0.91,0.15)	II	tail from (011) of IrO_2(100)-domain
	(0,1.0,0.15)		$(0,1)_S$ CTR from Ir(111)
	(0,1.47,0.15)	I	$(2\bar{2}0)$ of IrO_2(110)-domain
	(0,1.66,0.15)		(112) of IrO_2 powder
$H + K$ scan at $L = 0.15$ (not shown)	(0.43,0.43,0.15)		(110) of IrO_2 powder
	(0.80,0.80,0.15)		(211) of IrO_2 powder
	(0.86,0.86,0.15)	I + II	(002) of IrO_2(110) and of IrO_2(100)-domain
L scan at $(H,K) = (0, 0.73)$; Figure 5c	(0,0.73,0.33)		(110) of IrO_2 powder
	(0,0.73,1.51)		(101) of IrO_2 powder
	(0,0.73,2.1)	I	(200) of IrO_2(110)-domain
	(0,0.73,3.31)		(211) of IrO_2 powder
L scan at $(H, K) = (0, 0.91)$; Figure 5c	(0,0.91,0.5)		(101) of IrO_2 powder
	(0,0.91,1.51)		(200) of IrO_2 powder
	(0,0.91,2.14)		tail of $Ir(0,1,2)_S$ Bragg peak
	(0,0.91,3.0)	II	tail from (211) of IrO_2(100)-domain

[a] Note that the rutile structure fulfills the quasi selection rule for body centered tetragonal (bct) lattices, namely that the sum of $h + k + l$ for the rutile bulk Miller indices must be even for strong XRD Bragg reflections.

3.2. DFT Calculations. We now switch to the DFT calculations and thermodynamic analysis of the Ir oxidation. First, the oxygen chemisorption on Ir(111) was studied in a coverage range from 1/9 to 1 ML, and the calculated adsorption energies E_{ads} are given in Table 3 and plotted in Figure 7. Only oxygen adsorption at fcc-hollow sites was considered in the present calculations.[34] At low coverage of [1/9 ML, 1/4 ML], a slight attraction between adsorbates, which may be mediated through the substrate, is found. With increasing coverage, the (average) adsorption energy decreases monotonically due to the electrostatic (dipole) repulsion between the adsorbates, as reflected by the concomitant increase of the work function for instance by 0.18 eV (1/4 ML), 0.42 eV (1/2 ML), and 0.84 eV (2/3 ML), respectively. Destabilization of oxygen adsorption on Ir(111) at high coverage tends to facilitate the incorporation of oxygen into the subsurface region, preceding the formation of surface oxide and bulk oxide. The transition from chemisorption to bulk oxide will be initiated, according to King's theory, once the differential adsorption energy of oxygen on Ir(111) at a given coverage is less than the heat of formation of corresponding bulk oxide.[35,36] In Figure 7, the calculated differential adsorption energies at different coverages considered are plotted together with a horizontal line at −1.42 eV/O atom, the calculated heat of formation of bulk IrO_2 (rutile), which compares well with the experimental value of −1.29 eV/O.[37] It is found that the crossover occurs at coverage of 0.50 ML, namely, surface oxygen adsorption on Ir(111) is thermodynamic favorable when the coverage is less than 0.50 ML. Oxygen occupation in the subsurface region is energetically unfavorable. At a coverage of 0.50 ML, with a quarter ML of oxygen placed on subsurface tetrahedral sites, the total energy increased dramatically by about 2.8 eV per (2 × 2) cell. At higher coverage, however, the energy gain for further oxygen adsorption on the surface will be less than the energy gain for bulk oxide formation, and oxygen may penetrate into the subsurface region as a nucleation site for formation of the surface oxide and bulk oxide, respectively.

A O−Me−O trilayer with hexagonal symmetry was found to be a structural motif for surface oxides on various transition metal basal planes.[6,36,38] The optimized in-plane lattice constant of a free-standing O−Me−O trilayer is normally very different from that of the metal host. This generates certain superstructures, whose periodicity and detailed interfacial structures are determined by the intrinsic stability of the O−Me−O trilayer and the interfacial coupling between the O−Me−O trilayer and substrate underneath. In the present work, a single O−Ir−O trilayer with (6 × 6) hexagonal symmetry over a Ir(111)-(7 × 7) was identified by SXRD when oxygen partial pressure exceeds 10^{-3} mbar at 575 K or 1 mbar at 775 K. Full exploration of the huge unit cell is computationally demanding. Therefore the O-Me-O trilayer was approximated by IrO_2 with $(\sqrt{3} \times \sqrt{3})$ periodicity over Ir(111)-(2 × 2) surface (corresponding to oxygen coverage of 1.50 ML). It was found that the energetics of various O-Me-O trilayers considered are less sensitive to the detailed interfacial structures. Furthermore, the lower lying oxygen atoms tend to bond singly to the metal substrate underneath, which results from the preference of oxygen to bind to three and four metal atoms in metal oxides. Based on the insights obtained from this small supercell, calculations with realistic (6 × 6) trilayer lattice with coverage of 1.47 ML were performed. The optimized structure, shown schematically in Figure 3c, was used for the calculation of the X-ray structure factors and intensities in Figures 2b and 3a, where a good agreement with the experiment was achieved. The calculated adsorption energy of resultant structure is −1.17 eV/O.

For the Ir bulk oxide, there are two possible oxides known: rutile (IrO_2) and corundum (Ir_2O_3), as shown schematically in Figure 8. Calculated lattice constants for rutile IrO_2 are $a = 4.51$ Å and $c = 3.16$ Å, which agree well with experimental data of $a = 4.50$ Å and $c = 3.16$ Å from early report[39] and of $a = 4.52$ Å and $c = 3.16$ Å from the present study. For corundum Ir_2O_3, the calculated lattice constants are $a = 5.23$ Å and $c = 14.01$ Å, again in nice agreement with the experimental values of $a = 5.168$ Å and $c = 12.78$ Å derived from SXRD. Calculated heats of formation are −1.42 eV/O atom for IrO_2 and −0.70 eV/O atom for Ir_2O_3, respectively. A significantly larger heat of formation for rutile IrO_2 than for corundum Ir_2O_3 shows that the formation of rutile IrO_2 is thermodynamically more favorable than the corundum Ir_2O_3. This is in-line with the experimental finding that only rutile IrO_2 was formed at higher temperatures and higher pressures. The corundum Ir_2O_3 may however serve as a possible intermediate structure during the transition from the surface oxide to final bulk oxide. Indeed, a single O−Me−O trilayer is observed experimentally at 1 mbar at 575 K, and a multilayer oxide with similar hexagonal symmetry as the O−Me−O trilayer developed with increasing O_2 partial pressure to 100 mbar. The assignment

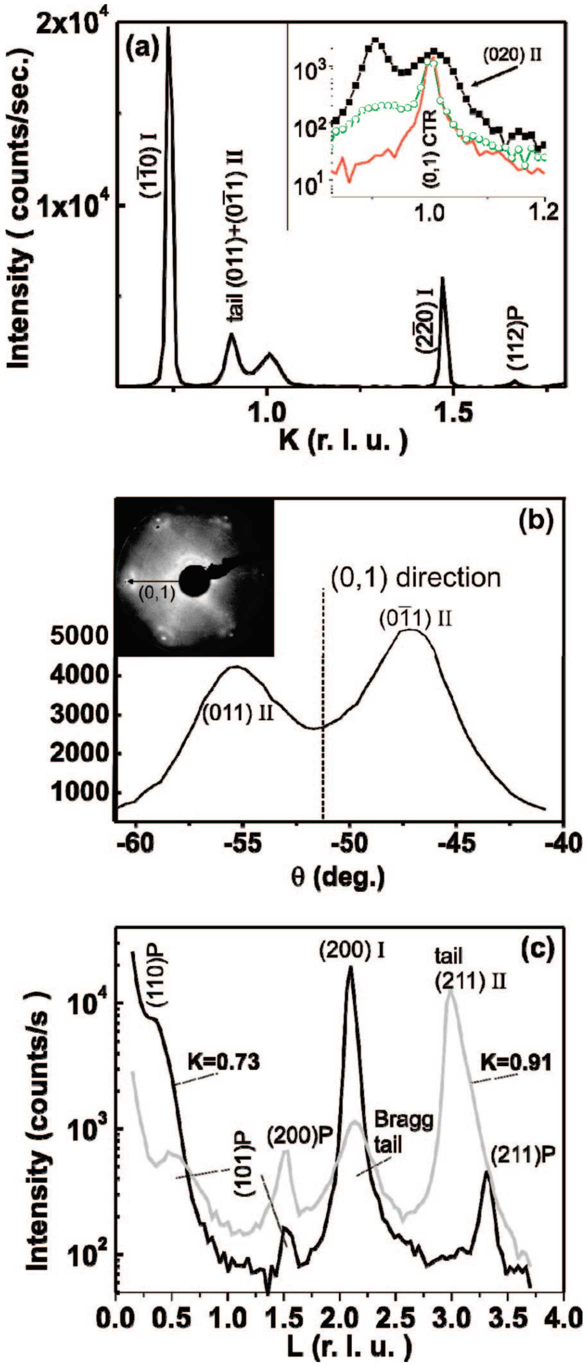

Figure 5. Formation of bulk IrO_2 on Ir(111) at 100 mbar O_2 and 875 K as revealed by SXRD. The reflections from domains I and II are labeled with indices in real-space IrO_2 bulk coordinates, in addition to the polycrystalline component "P". (a) In-plane K scan with the predominant (1$\bar{1}$0) reflection from domain I. In the inset a zoom in for the region close to $K = 1$ is shown (filled squares). For comparison the signal from the clean surface (solid/red line) is given, in addition to the signal from the multilayer hexagonal oxide (open/green circles). When IrO_2 bulk oxide forms, an additional peak grows at $K = 1.04$ close to the substrate (0,1) CTR reflection, corresponding to the (020) reflection from domain II. (b) Rocking scan at (0, 0.91, 0.15): two overlapping reflections are observed, which are symmetrical with respect to the $(0,1)_S$ direction, corresponding to (011) type reflections of domain II. In the inset a LEED pattern obtained after NO_2 oxidation is shown, which exhibits the same splitting of the reflections. (c) L scans at $H = 0$, $K = 0.73$ (black line) and K=0.91 (gray line). All reflections can be indexed as described in the text.

of the multilayer oxide to a corundum-like oxide is reasonable, since corundum $Ir_2O_3(0001)$ has hexagonal symmetry.

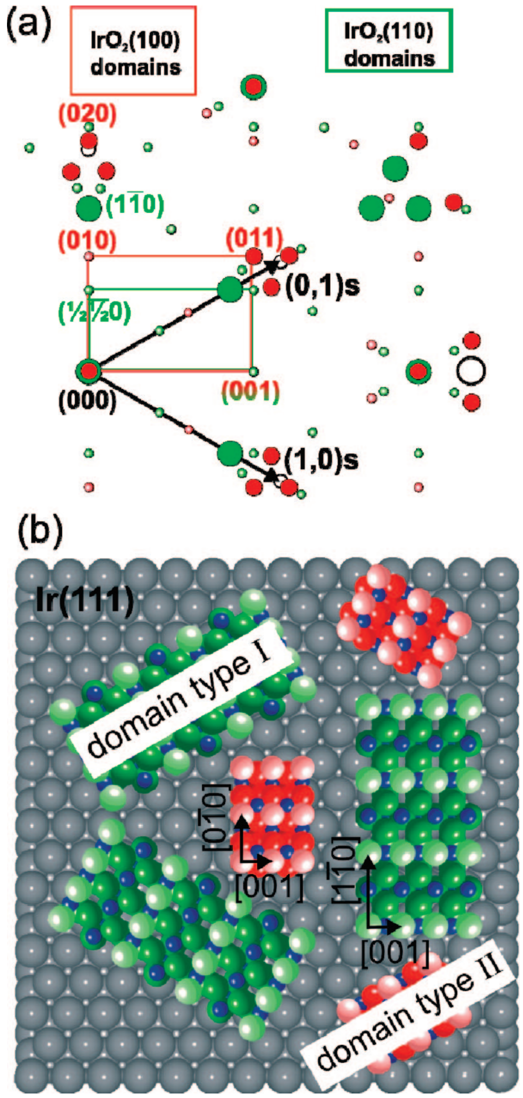

Figure 6. (a) In-plane reciprocal lattice of the bulk IrO_2(110)- and (100)-oriented domains. The big green and red solid circles represent respectively strong in-plane Bragg peaks from IrO_2 (110)- and (100)-oriented domains. The small symbols (green for the (110) domains and red for the (100) domains) correspond to CTRs or Bragg peaks from oxygen only, which are too low in intensity to be detected by SXRD. All indices are given in IrO_2 bulk coordinates. The black open circles correspond to substrate CTRs or in plane Bragg reflections. The substrate reciprocal lattice vectors are indicated by the arrows. (b): Illustration of the formation of bulk IrO_2 (110) and (100) domains on the Ir(111) in real space. The orientations of the IrO_2 (110) and (100) domains with respect to the Ir(111) substrate (epitaxial relation) are as given in the text.

TABLE 3: Calculated Average Adsorption Energy of Different Structures from Chemisorptions to Surface Oxides[a]

structures	E_{ads}	structures	E_{ads}
chemisorptions		chemisorptions	
1/9 ML	−1.85	3/4 ML	−1.40
1/4 ML	−1.92	1.00 ML	−0.92
1/3 ML	−1.78	surface oxide	
1/2 ML	−1.70	1.47 ML (6 ×)/(7 × 7)	−1.17
2/3 ML	−1.50	1.50 ML (r3 × r3)/(2 × 2)	−1.26

[a] The unit is eV per oxygen atom.

The phase diagram for the oxidation of Ir(111) including the structures discussed above is shown in Figure 9, where a vertical dashed line at −1.42 eV indicates the thermodynamic preference of formation of bulk IrO_2 (rutile). The chemisorption phases

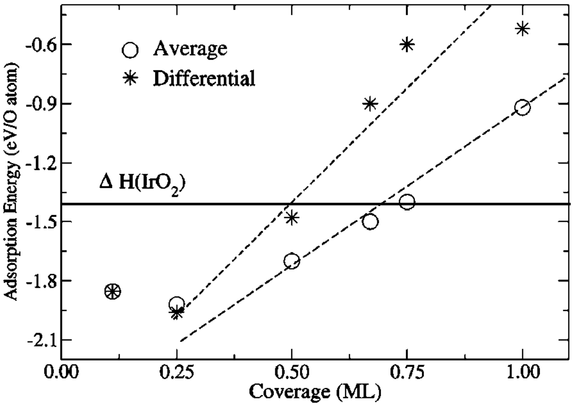

Figure 7. Calculated average adsorption energy (open circle) and differential adsorption energy (star) for oxygen adsorption on the Ir(111) surface at coverages of [1/9 ML, 1 ML]. The horizontal line is the calculated heat of formation of bulk ruitle IrO_2 oxide, and dashed lines are plotted to guide the eye.

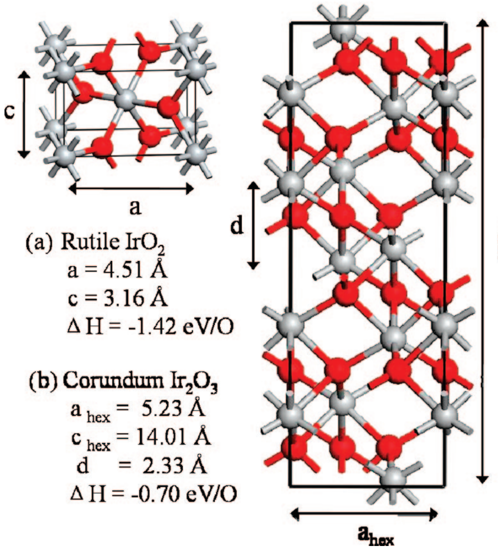

Figure 8. Schematic ball-stick structures of bulk rutile IrO_2 (a) and corundum Ir_2O_3 (b) oxides with calculated lattice constants and heat of formation per oxygen. The red and gray spheres represent O and Ir atoms, respectively.

are the only stable structures before the formation of bulk oxide is thermodynamically favorable. The single (6 × 6) O−Me−O trilayer oxide identified above constitutes a meta-stable structure, which is stabilized for kinetic reasons, consistent with the experimental findings. At low temperatures (e.g., 575 K), the transition from the chemisorption phase to the bulk oxide is comparably slow, and single O−Ir−O trilayer and multilayer oxide can be formed by gradually increasing the oxygen partial pressure. The calculated transition O_2 partial pressure from the chemisorption phases ($\theta = 0.50$ ML) to the O-Me-O trilayer ($\theta = 1.47$ ML) is 10^{-2} mbar at 575 K (equivalent to $\Delta\mu = -0.90$ eV), which falls well into the experimental pressure window of 10^{-3} mbar to 1mbar (Table 1) for the formation of single O−Ir−O trilayer. At higher temperatures (775K and above), the transition from the chemisorption phase to bulk oxide via meta-stable states is facilitated. Indeed, as found in the experiments (Table 1), the pressure window for the formation of single O−Me−O trilayer is narrower, and even the formation of multilayer oxide cannot be captured experimentally. Finally, the $\sqrt{3} \times \sqrt{3}$R30° trilayer structure is not observed experimentally, similar to the oxidation of Pt(111)[40] and Ag(111).[41]

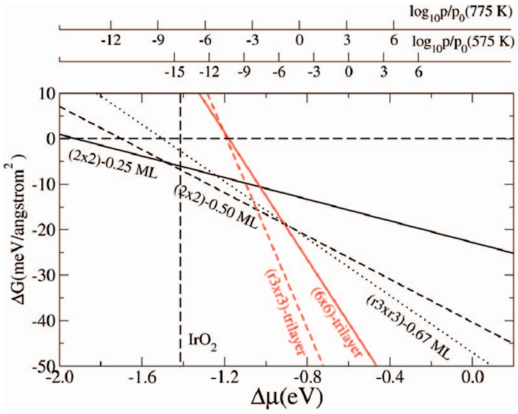

Figure 9. (Bottom) Calculated phase diagram for oxidation of Ir(111), where only favorable structures have been included for simplicity. The vertical dashed line at −1.42 eV (heat of formation of rutile IrO_2) indicates the condition for the formation of bulk oxide. (Top) Corresponding oxygen partial pressures at 575 and 775 K are indicated for comparison with experiments.

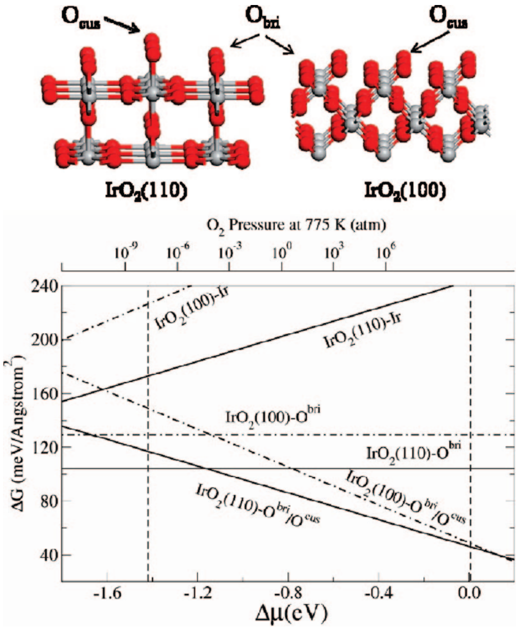

Figure 10. (Bottom) Calculated phase diagram for rutile IrO_2 (110) and (100) surfaces with different terminations: Ir-termination, O-bri-termination and O-bri/O-cus-termination. The vertical dashed line (left) at −1.42 eV represents the lower limit of stable bulk oxide. (Top) Schematic ball-stick structures of rutile IrO_2 (110) and (100) surfaces. The red and gray spheres represent O and Ir atoms, respectively.

At high temperature (775 K) and higher O_2 partial pressure, the experiments give ample evidence for the formation of bulk rutile IrO_2 with (110) and (100) orientations. Since no structural information about the termination of the oxide islands could be provided by the SXRD experiments, we have performed density functional theory calculations supplemented with thermodynamic analysis[24] to determine possible (stable) surface terminations. Symmetric surfaces with various terminations, Ir-termination, O-bridge(bri) termination (stoichiometric) and O-bri /O-coordinativley unsaturated (cus) termination (fully oxygen covered), were modeled by seven metal layer thick slabs, and the atoms in the first Ir−O layer, O-bri and O-cus on both sides were allowed to relax to their equilibrium positions. The structures are shown schematically in the top of Figure 10. For IrO_2(110) and (100) surfaces, calculated in-plane lattice constants in (1 × 1) cell are (3.16 Å × 6.38 Å) and (3.16 Å ×

4.51 Å), whereas *d* spacings between adjacent Ir layers are 3.19 and 2.25 Å, respectively. These data are in excellent agreement with experimental results for the (110)- and (100)-oriented domains of the IrO_2 film with in-plane lattice constants (3.16 Å × 6.39 Å) and (3.16 Å × 4.52 Å), and *d* spacings of 3.17 and 2.22 Å, respectively. The relative stability of (110) and (100) orientated surfaces with various terminations was calculated and is shown in the bottom of Figure 10. From this plot, it is immediately seen that for both (110) and (100) surfaces, the surfaces with oxygen termination (O-bridge and O-cus) are dominating over a wide range of oxygen chemical potential. More importantly, it is found that the relative difference of the surface energy between (110) and (100) surfaces with oxygen terminations is modest (less than $\sim$25 meV/ Å^2). The preferred growth of (110) IrO_2 domains is very likely related to the lower interfacial energy for this type of domains, which was ignored here.

4. Conclusion

In summary, we have studied the oxidation of the Ir(111) surface in O_2 pressure range of 10^{-6} mbar up to ambient pressure by in situ SXRD using a dedicated UHV/high pressure chamber. At 575 K and an O_2 partial pressure of $10^{-3}-1$ mbar, a hexagonal O−Ir−O trilayer forms on the Ir(111) surface, resembling the initial oxidation of the Rh(111).[6] Increasing the pressure to 100 mbar leads to the formation of the O−Ir−O trilayer on which a hexagonal multilayer oxide with a corundum Ir_20_3 structure grows. The hexagonal multilayer oxide is a metastable precursor toward the bulk oxide formation. According to the DFT calculations, both the trilayer and multilayer surface oxides are thermodynamically not stable with respect to the bulk rutile IrO_2, and are thus considered to be transient and kinetically stabilized structures. At higher temperatures (775 K or above), the O−Ir−O trilayer surface oxide forms at intermediate pressures (around 1 mbar) and transforms at higher pressures (around 100 mbar) into bulklike rutile IrO_2, exhibiting predominantly (110)- and (100)-oriented domains. The oxidation of the Ir(111) follows the general trend for oxidation of the late transition metals in that the formation of a few-atomic-layer-thin, so-called surface oxide, precedes the bulk oxidation.

Acknowledgment. We acknowledge partial financial support from the European Union under Contract No. NMP3-CT-2003-505670 (NANO2). We thank R. Weigel for technical support during the synchrotron radiation measurements at ANKA. WXL was supported by NSFC (20503030, 20733008) and MOST 2007CB815205.

References and Notes

(1) Lundgren, E.; Mikkelsen, A.; Andersen, J. N.; Kresse, G.; Schmid, M.; Varga, P. *J. Phys.: Condens. Matter* **2006**, *18*, R481.

(2) Lundgren, E.; Over, H. *J. Phys.: Condens. Matter* **2008**, *20*, 180302.

(3) Stierle, A.; Molenbroek, A. M. *MRS Bull.* **2007**, *32*, 1001.

(4) Over, H.; Kim, Y. D.; Seitsonen, A. P.; Wendt, S.; Lundgren, E.; Schmid, M.; Varga, P.; Morgante, A.; Ertl, G. *Science* **2000**, *287*, 1474.

(5) He, Y. B.; Knapp, M.; Lundgren, E.; Over, H. *J. Phys. Chem. B* **2005**, *109*, 21825.

(6) Gustafson, J.; Mikkelsen, A.; Borg, M.; Lundgren, E.; Köhler, L.; Kresse, G.; Schmid, M.; Varga, P.; Yuhara, J.; Torrelles, X.; Quirós, C.; Andersen, J. N. *Phys. Rev. Lett.* **2004**, *92*, 126102.

(7) Lundgren, E.; Kresse, G.; Klein, C.; Borg, M.; Andersen, J. N.; De Santis, M.; Gauthier, Y.; Konvicka, C.; Schmid, M.; Varga, P. *Phys. Rev. Lett.* **2002**, *88*, 246103.

(8) Hendriksen, B. L. M.; Frenken, J. W. M. *Phys. Rev. Lett.* **2002**, *89*, 046101.

(9) Burch, R.; Breen, J. P.; Meunier, F. C. *Appl. Catal., B* **2002**, *39*, 283.

(10) Liu, Z. P.; Jenkins, S. J.; King, D. A. *J. Am. Chem. Soc.* **2004**, *126*, 10746.

(11) Chan, C. M.; Weinberg, W. H. *J. Chem. Phys.* **1979**, *71*, 2788.

(12) Ivanov, V. P.; Boreskov, G. K.; Savchenko, V. I.; Egelhoff, W. F.; Weinberg, W. H. *Surf. Sci.* **1976**, *61*, 207.

(13) Zhdan, P. A.; Boreskov, G. K.; Boronin, A. I.; Egelhoff, W. F.; Weinberg, W. H. *Surf. Sci.* **1976**, *61*, 25.

(14) Hagen, D. I.; Nieuwenhuys, B. E.; Rovida, G.; Somorjai, G. A. *Surf. Sci.* **1976**, *57*, 632.

(15) Marinova, T. S.; Kostov, K. L. *Surf. Sci.* **1987**, *185*, 203.

(16) Davis, J. E.; Nolan, P. D.; Karseboom, S. G.; Mullins, C. B. *J. Chem. Phys.* **1997**, *107*, 943.

(17) Conrad, H.; Küppers, J.; Nitschké, F.; Plagge, A. *Surf. Sci.* **1977**, *69*, 668.

(18) Bernard, P.; Peters, K.; Alvarez, J.; Ferrer, S. *Rev. Sci. Instrum.* **1999**, *70*, 1478.

(19) Stierle, A.; Steinhauser, A.; Ruhm, A.; Renner, F. U.; Weigel, R.; Kasper, N.; Dosch, H. *Rev. Sci. Instrum.* **2004**, *75*, 5302.

(20) Hammer, B.; Hansen, L. B.; Nørskov, J. K. *Phys. Rev. B* **1999**, *59*, 7413.

(21) Perdew, J. P.; Chevary, J. A.; Vosko, S. H.; Jackson, K. A.; Pederson, M. R.; Singh, D. J.; Fiolhais, C. *Phys. Rev. B* **1992**, *46*, 6671.

(22) Monkhorst, H. J.; Pack, J. D. *Phys. Rev. B* **1976**, *13*, 5188.

(23) The vacuum region was 14 Å to prevent unphysical coupling between two adjacent films through the vacuum, and dipole correction was applied since oxygen adsorbed at one side of the slab.

(24) Reuter, K.; Scheffler, M. *Phys. Rev. B* **2001**, *65*, 035406.

(25) Li, W.-X.; Stampfl, C.; Scheffler, M. *Phys. Rev. Lett.* **2003**, *90*, 256102.

(26) Weast, R. C. *CRC Handbook of Chemistry and Physics*, 55th ed.; CRC Press:Cleveland, OH, 1974−1975.

(27) (a) The amplitude of the structure factor was obtained from rocking scans after background subtraction and application of standard correction factors. (b) Vlieg, E. *J. Appl. Crystallogr.* **1997**, *30*, 532.

(28) He, Y. B.; Seitsonen, A. P.; Over, H. In preparation, 2008.

(29) Note that the structural perfection of the surface oxide layer is too low to perform a full crystallographic analysis of the interfacial structure. Nevertheless, the recorded data are in good agreement with the structure factor calculated using the trilayer model put forward by theory.

(30) Concurrently, the peak in the $H + K$ scan shifts from $H = K = 0.87$ for low O_2 pressure to 0.91 (not shown here).

(31) The observed reflection at (0,0.91,0) corresponds to the corundum $(11\bar{2}0)$ reflection and the reflection at (0,0.91,3.12) corresponds to the corundum $(11\bar{2}6)$ reflection.

(32) The real space in-plane lattice constants along the [001] and $[1\bar{1}0]$ directions can be derived as $2\pi/[2.672 \times\sqrt{3}\times(0.86/2)] = 3.16$ Å and $2\pi/[2.672 \times (0.735/2)] = 6.39$ Å, respectively.

(33) Assmann, J.; Crihan, D.; Knapp, M.; Lundgren, E.; Löffler, E.; Muhler, M.; Narkhede, V.; Over, H.; Schmid, M.; Seitsonen, A. P.; Varga, P. *Angew. Chem. Int. Ed.* **2005**, *44*, 917.

(34) Xu, Y.; Mavrikakis, M. *J. Chem. Phys.* **2002**, *116*, 10846.

(35) Carlisle, C. I.; Fujimoto, T.; Sim, W. S.; King, D. A. *Surf. Sci.* **2000**, *470*, 15.

(36) Todorova, M.; Li, W. X.; Ganduglia-Pirovano, M. V.; Stampfl, C.; Reuter, K.; Scheffler, M. *Phys. Rev. Lett.* **2002**, *89*, 096103.

(37) Landolt-Boernstein, 2001; New Series Vol. IV/19A4.

(38) Reicho, A.; Stierle, A.; Costina, I.; Dosch, H. *Surf. Sci.* **2007**, *601*, L19.

(39) Bolzan, A. A.; Fong, C.; Kennedy, B. J.; Howard, C. J. *Acta Cryst. B* **1997**, *53*, 373.

(40) Ellinger, C.; Stierle, A.; Robinson, I. K.; Nefedov, A.; Dosch, H. *J.Phys.: Condens. Matter* **2008**, *20*, 184013.

(41) Schmid, M.; Reicho, A.; Stierle, A.; Costina, I.; Klikovits, J.; Kostelnik, P.; Dubay, O.; Kresse, G.; Gustafson, J.; Lundgren, E.; Andersen, J. N.; Dosch, H.; Varga, P. *Phys. Rev. Lett.* **2006**, *96*, 146102.

JP803607Y